CRYSTAL GROWTH & DESIGN

pubs.acs.org/crystal

Article

Enhanced Easy Axis Magnetic Anisotropy in a Siloxane-Bridged Linear Co^{II}_3 Single-Molecule Magnet

Published as part of Crystal Growth & Design special issue "Frontiers of Molecular Magnetism".

Madhuri Bhattacharya, Sunil Kumar, Björn Schwarz,* Liviu Ungur,* and Kartik Chandra Mondal*

Cite This: *Cryst. Growth Des.* 2025, 25, 7085−7096

Read Online

ACCESS | Metrics & More | Article Recommendations | Supporting Information

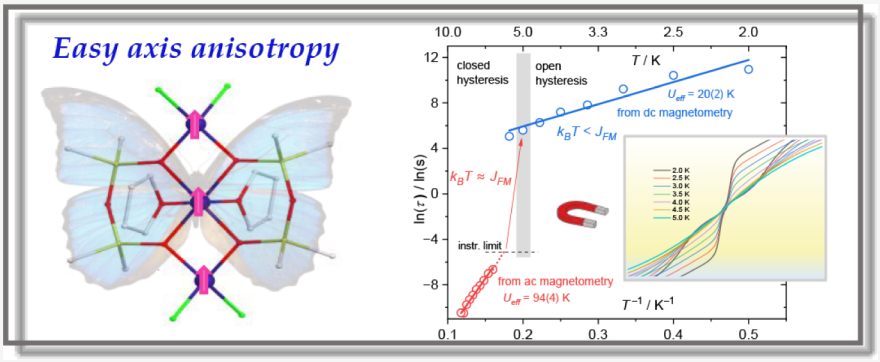

ABSTRACT: A novel ferromagnetically coupled dianionic linear Co^{II}_3 complex has been synthesized and characterized as a potential single-molecule magnet (SMM) with enhanced axial magnetic anisotropy. This complex features three Co^{II} ions out of which one Co^{II} ion adopts an octahedral geometry and two other Co^{II} ions adopt tetrahedral coordination geometries. The Co^{II} ions are bridged by two siloxane dianions in a η^2:η^2:μ_3 fashion leading to a butterfly-like molecular structure, which has been studied by magnetic susceptibility measurements. Computational analysis using OpenMOLCAS, CASSCF, and CASPT2 methods revealed ferromagnetic (FM) exchange coupling between the neighboring Co^{II} ions of about +10.2 cm^{-1} and strong axial anisotropy parallel to the Co−Co axis for the ground exchange states. From *ab initio* POLY-ANISO analysis, a total magnetization blocking barrier of about 70 cm^{-1} (101 K) and strongly reduced probabilities for quantum tunneling due to FM coupling were predicted. Magnetic ac susceptibility measurements revealed slow magnetic relaxation via an Orbach relaxation process with U_{eff} = 94(4) K and τ_0 = 4(2)×10^{-10} s (fitted from 8.5 to 6.25 K). Below 5 K, a pinched open hysteresis can be observed that opens more when approaching 2 K, indicating very slow magnetic relaxation in this temperature range in agreement with the predicted small quantum tunneling probabilities. These very slow magnetic relaxation times were further investigated by time-dependent dc magnetometry. Our study presents the first report on the influence of siloxane bridge binding on the SMM property of Co^{II} nuclei by in-depth theoretical analysis and experimental susceptibility measurements, indicating the design of improved materials.

INTRODUCTION

Single-molecule magnets (SMMs) represent a paradigm shift in the understanding of magnetic materials, exhibiting slow relaxation of magnetization at the molecular level.[1] This property arises from the coupling of the intrinsic ground state spin (S) of the individual molecule with its magnetic anisotropy (D). When $S \geq 1$, the combined effect of low-symmetry crystal field and strong spin−orbit coupling gives rise to the zero-field splitting (ZFS), characterized by the D parameter, which creates an energy barrier that stabilizes the magnetic moment in one of the two orientations ($+M_s$ and $-M_s$) (Figure 1).[2] As a result, SMMs can retain their magnetic information at low temperatures either as spin-up or spin-down state, making them potential candidates for applications in high-density data storage,[3] quantum computing,[4] and spintronics.[5] Generally, most SMMs are polynuclear Mn^{III}-based complexes,[3,6] starting first with $[Mn_{12}O_{12}(OAc)_{16}(H_2O)_4]\cdot 2HOAc\cdot 4H_2O$, i.e., "$Mn_{12}$−Ac," by Boyd et al. in 1988.[7] SMM performance is characterized mainly by two parameters: the effective energy barrier for magnetization reversal (U_{eff}) and the magnetic blocking temperature (T_B).[8] Designing a SMM with exchanged bias and collinear/parallel arrangements of the

Received: January 9, 2025
Revised: May 9, 2025
Accepted: May 12, 2025
Published: May 20, 2025

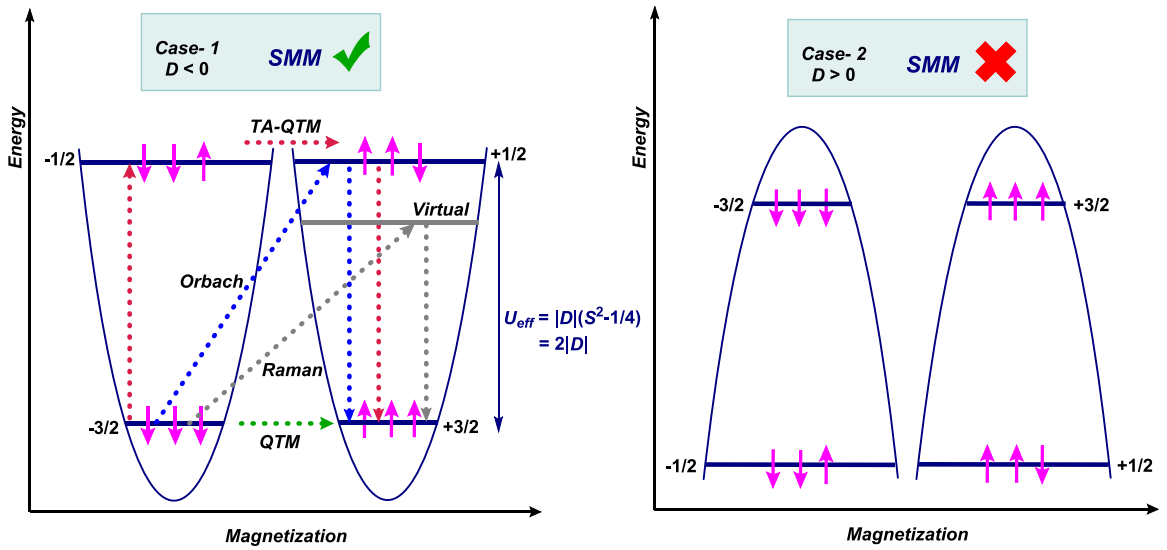

Figure 1. Schematic representation of two types (positive and negative) of zero-field splitting for $S = 3/2$ system in a double-well energy diagram. Case 1 includes the possible spin−lattice relaxation pathways in SMMs where the thick navy blue lines represent the spin states. The gray line represents a virtual state by which Raman relaxation proceeds. Color code: green = ground state QTM, red = thermally assisted QTM (TA-QTM), blue = Orbach relaxation, gray = Raman relaxation.

local magnetic easy axis is highly desired for achieving a high energy barrier of magnetization reversal.

The reversal of magnetization or spin reorientation in SMM via an energy barrier that is accompanied by thermal energy transfer from the "spin system" to the "lattice system" (and vice versa) is called spin−lattice relaxation (Figure 1).[1] Here the most studied Orbach relaxation mechanism follows an Arrhenius law: $\tau = \tau_0 \exp(U_{eff}/k_BT)$, where U_{eff} is related to S^2 and the ZFS parameter (D) [$U_{eff} = |D|S^2$ for integer spin and $U_{eff} = |D|\left(S^2 - \frac{1}{4}\right)$ for half-integer spin]. It was theoretically predicted that increasing $S > 12$ will not enhance the energy barrier, as the D value is inversely related to S^2 partially due to the random orientation of the easy axis of magnetization.[9] Thus, research is now focusing on increasing the D value of a single ion. In this regard, the lanthanide ions, with large single-ion magnetic anisotropy (D), are promising candidates, which have reported energy barriers of nearly up to 695 cm^{-1}.[10−12] A dysprosium metallocene-based single-ion magnet (SIM), reported in 2018, achieved magnetic hysteresis at liquid nitrogen temperature (80 K), with U_{eff} = 1541 cm^{-1}.[13] However, strong couplings in lanthanide-based systems are challenging to achieve without air-sensitive radical bridges,[14,15] which may limit their usability in practical applications. This has renewed interest in transition metal ion chemistry with easier magnetic couplings.[2]

In the literature, polynuclear transition metal complexes displaying SMM properties are mainly reported with Mn, Fe, Cu, and their mixed metallic complexes, whereas Co and Ni-based SMMs are reported to a lesser extent.[16−18] The challenges lie in designing coordination environments that enhance this anisotropy while maintaining structural stability. Moreover, in polynuclear SMMs, retaining the magnetic anisotropy is difficult due to the possible antiferromagnetic (AFM) couplings between the metal centers, compared to mononuclear SMMs (also called SIMs). Since the past two decades, several trinuclear Co^{II} complexes with N-/O-based ligands have been reported, and a comparison of their structural and magnetic properties is provided in Table S1. A recent Co^{II}_3 complex reported by Zabala-Lekuona et al.[19] [{Co(μ-N_3O_3L)}$_2$Co], where $N_3O_3H_3L$ is derived from 1,1,1-tris(aminomethyl)ethane and salicylaldehyde, consists of a very short intramolecular Co···Co distance of 2.909 Å in octahedral geometry, which leads to a strong antiferromagnetic exchange coupling ($J = -6.38$ cm^{-1}) and high local anisotropic splitting parameter ($D = -146.0$ cm^{-1}). This contributed mainly to the quenching of QTM and observation of SMM behavior at a zero dc field. In contrast, another interesting complex, [(baron^{Me})Co^{II}_3], where baron^{Me} is a triplesalophen ligand, having Co^{II} in tetrahedral geometry and Co···Co intramolecular distance greater than intermolecular distance, showed strong ferromagnetic coupling (J = +5.23 cm^{-1}) through π overlap with the bridging phloroglucinol; however, lacked SMM properties.[20] Additionally, a series of Co^{II}_3 complexes synthesized with Mannich−Schiff-base ligands feature Co^{II} in octahedral geometry with positive D-value, and hence no SMM property.[21] Monakhov et al.[22] reported a Co^{II}_3 complex [{CoN(SiMe$_3$)$_2$(μ-η-[o-C_6H_4(kNSi^{i}Pr$_3$)$_2$])}$_2$Co] where the central Co^{II} resides in a sandwiched geometry, leading to a high effective energy barrier, U_{eff} = 33.4(8) cm^{-1}. Among these, most of the Co^{II} centers have octahedral geometry, with high magnetic anisotropy (D)[19] up to −146.0 cm^{-1} and strong spin−orbit coupling constant (J)[21] up to +9.74 cm^{-1}. Herein, we present the synthesis, crystal structure, and complete characterization of a trinuclear Co^{II} complex (**2**) in a new framework, namely, siloxane ligand bridging. Alongside, we investigated its magnetic properties by in-depth *ab initio* theoretical analysis and experimental susceptibility measurements by both direct current (dc) and alternating current (ac) methods.

RESULT AND DISCUSSION

The reaction of the CDP ligand (**1**) with $(Ph_3P)_2CoCl_2$ in toluene led to the formation of a faded blue precipitate, which was filtered out and further reacted with two more equivalents of CDP in THF to obtain greenish-blue needles of [(HCDP)$_2Co^{II}_3$(sil)$_2Cl_4$(THF)$_2$]·4THF (**2**) via silicone grease activation in 20% yield (Scheme 1) [CDP = $(Ph_3P)_2C$

https://doi.org/10.1021/acs.cgd.5c00037
Cryst. Growth Des. 2025, 25, 7085−7096

Scheme 1. Synthesis of Co^{II}_3-Complex 2

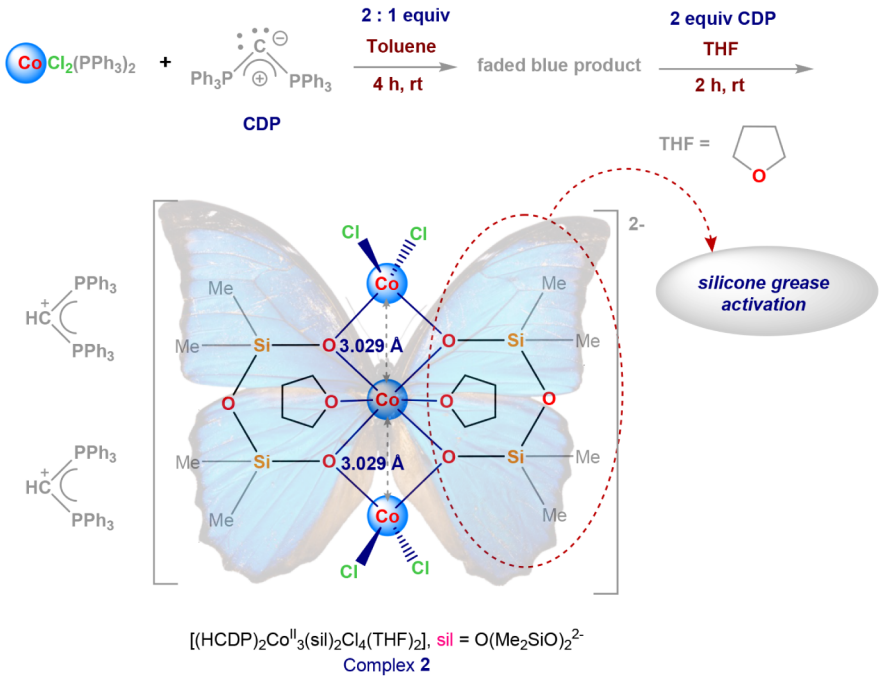

possessing two pairs of electrons on the central C(0) atom]. The super basic CDP ligands abstracted a proton even from an organic solvent like THF and are present as two counter cations in **2**, promoting siloxane bridging in the dianionic Co^{II} trinuclear core. The reaction was carried out under an inert argon atmosphere to avoid the formation of undesired Co^{III} species.

The UV−visible spectrum (Figure S5) of **2** from 350 to 900 nm in a THF (blue-colored) solution showed absorption bands with λ_{max} of 596 and 676 nm. Complex **2** has been characterized by FT-IR spectroscopy using KBr pellet (Figure S6), where the characteristic peaks appeared are (υ_{stret}, cm^{-1}): 3055 for C═P; 2960 for aromatic C−H; 2839 to 2680 for aliphatic C−H (from the methyl group of siloxane); 1109 for Si−O−Si; 1025 for C−O; 994 for Si−O; and 502 for Co−Cl. We have performed X-band (9.45 GHz) EPR spectra of **2** in DMSO at 298 and 77 K; however, no signal was detected in both conditions (Figures S8 and S9).

Description of Structure. The complex $[(HCDP)_2Co^{II}_3(sil)_2Cl_4(THF)_2]\cdot 4THF$ (**2**) crystallizes in the triclinic *P*-1 space group (see Tables S2−S4 for structural parameters). The structure of **2** consists of a linear trinuclear Co^{II}_3 unit with a center of inversion (*i*) present at the central Co^{II} (hereafter named Co1) metal ion (Figure 2). Within this centrosymmetric anionic arrangement, the three Co^{II} ions are connected by two $\eta^2{:}\eta^2{:}\mu_3$-siloxane, i.e., $O(Me_2SiO)_2^{2-}$ bridges, creating a butterfly-type structure where a Co−Co−Co unit lies along the body of the butterfly and two $O(Me_2SiO)_2^{2-}$ ligands reside on two wings (Scheme 1). The structure can be considered as a combination of a dianionic octahedral $Co\{(THF)O(Me_2SiO)_2\}_2^{2-}$ ion in the middle, which is doubly bonded to two neutral terminal $CoCl_2$ units [Co2/Co2′] on both sides. Each outer cobalt nucleus (Co2 and Co2′) is ligated with two terminal chloride ligands and two oxygen atoms of the two siloxane ligands, thus adopting a distorted tetrahedral $[O_2Cl_2]$ coordination environment. The central Co1, which resides on an inversion center, displays an

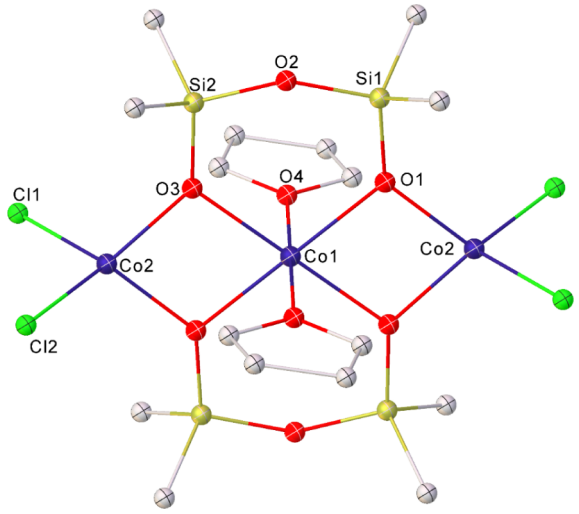

Figure 2. Molecular structure of the $[Co^{II}_3(sil)_2Cl_4(THF)_2]^{2-}$ core of the complex $[(HCDP]_2Co^{II}_3(sil)_2Cl_4(THF)_2]\cdot 4THF$ (**2**). sil = $O(Me_2SiO)_2^{2-}$. Four lattice THF molecules, two HCDP moieties, and H atoms were omitted for clarity. Colors: Co, blue; Si, yellow; Cl, green; O, red; C, gray. HCDP = $(Ph_3P)_2CH$, Ph = C_6H_5, and Me = CH_3. Selected bond lengths (Å) and bond angles (°): Cl1−Co2 2.278(3), Cl2−Co2 2.291(3), Co1−O3 2.061(6), Co1−O1 2.069(6), Co1−O4 2.200(7), Si1−O1 1.601(6), Si1−O2 1.625(7); Cl1−Co2−Cl2 104.55(11), O3−Co1−O4 89.7(3), O1−Co2−Cl1 117.21(19), Co2−O1−Co1 97.7(2).

axially elongated octahedral geometry, with an $[O_6]$ coordination environment formed by four siloxane O atoms and two O atoms of the two THF moieties. The bond distance of the apical Co1−O4/O4′ [2.200(7) Å] is significantly longer than the equatorial distances [Co1−O1/O3 = 2.069(6)−2.061(6) Å], which are typical of Co^{II} complexes with O donors due to the Jahn−Teller distortion. The bond angle of inner O1−Co2−O3′ is 85.0(2)°, whereas outer Cl1−Co2−Cl2 is 104.55(11)°. The shortest intramolecular Co1···Co2 and

https://doi.org/10.1021/acs.cgd.5c00037
Cryst. Growth Des. 2025, 25, 7085−7096

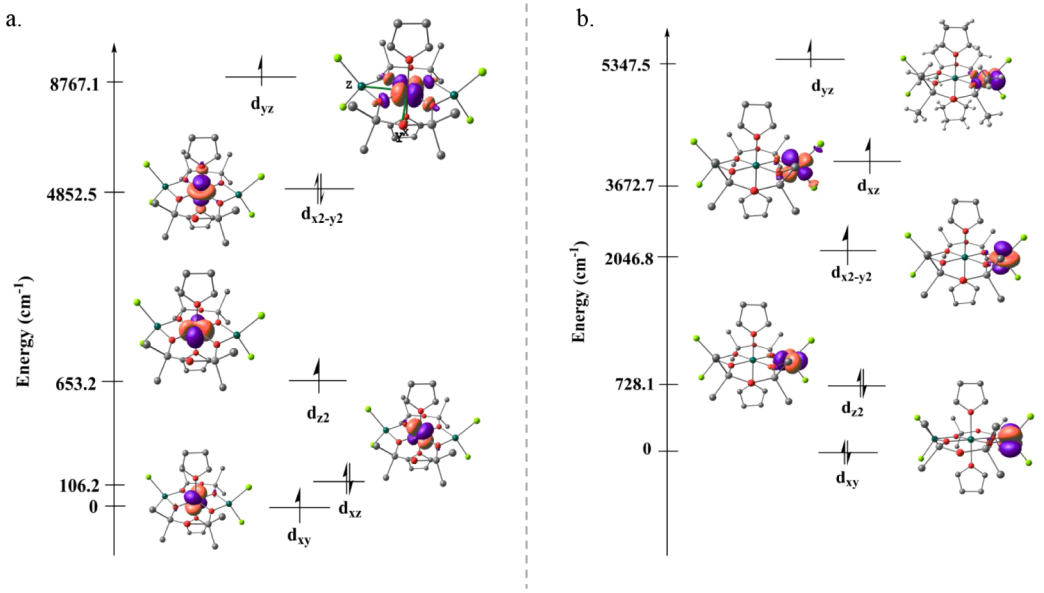

Figure 3. The d-orbital splitting for the central Co^{II} ion in the octahedral ligand field environment (a) and the terminal Co^{II} ion in the tetrahedral ligand field environment (b).

Co2···Co2′ distances are 3.029 and 6.058 Å, respectively, which are in the comparable range known for Co_3 complexes with SMM behavior (Table S1). Crystal packing layers of the Co_3 core in **2** are viewed along different directions, where each molecule of **2** is well separated from the others with the shortest intermolecular distance of 10.946 Å between Co1 ions of the two neighboring molecules (Figure S4). However, supramolecular interactions like H-bonding and π-interactions are not found in this complex. The bridging angles Co1−O1−Co2 and Co1−O3−Co2 are nearly 97.7(2)°, which are considerably small due to the proximity of Co centers, desirable for well-exchange coupling interactions. The angle P1−C1−P2 around the central C atom of the cationic HCDP moiety is bent to 127.8(6)°, indicating sp^2 hybridization. The angle Co2−Co1−Co2′ is 180°, suggesting a linear arrangement.

Magnetic Properties: *Ab Initio* Calculations. In order to acquire a deeper understanding of the electronic and magnetic structures of complex **2**, we conducted a thorough *ab initio* investigation employing X-ray molecular structure analysis. We executed *ab initio* multiconfigurational complete active space self-consistent field (CASSCF and CASPT2) calculations utilizing the OpenMolcas software package,[23] while density functional theory calculations were performed using the ORCA 5.0.4 software package.[24]

The first goal of the *ab initio* investigation was to establish the ground state spin of the entire compound and the local spins on individual Co sites in **2**. We found that the ground state of the entire Co^{II}_3 complex (**2**) is $S = 9/2$, confirmed by all DFT calculations with different functionals (B3LYP, PBE, TPSS0, and wB97) (Table S6). This finding suggests that all three Co sites have ground spin states $S = 3/2$ coupled by a strong ferromagnetic interaction. The Loewdin charge (+0.565714) on the central octahedral Co^{II} ion of **2** is significantly higher than those of two terminal tetrahedral Co^{II} ions (+0.26997). The spin population analysis shows around ∼2.7 due to three unpaired electrons on each Co^{II} ion (Table S7). The negative Loewdin charge on each O atom of the Co−O−Co unit of the dianionic siloxane $(Me_4Si_2O_3)^{2-}$ bridge is around −0.40, while the corresponding Si atom possesses a positive Loewdin charge of +0.56. The Loewdin charge on each Cl atom is −0.41. Thus, the dianionic siloxane ligands are expected to provide a favorable ligand field, leading to axial local magnetic anisotropy at each Co^{II} ion.

The second goal of the theoretical investigation was to establish the local electronic structure and magnetic anisotropy of each Co^{II} site. The electronic structure of each mononuclear Co^{II} fragment of the trinuclear Co_3 unit was calculated by substituting the other two Co^{II} ions with Zn^{II} ions. A series of DFT calculations revealed that the total ground state on each Co^{II} atom is a $3d^7$ configuration, high-spin ($S = 3/2$) (Tables S8 and S9). After confirming this, we performed multireference CASSCF/CASPT2 calculations for individual Co sites, i.e., on three isostructural Zn_2Co equivalents of **2**. For each Co site, 10 states $S = 3/2$ and 40 states $S = 1/2$ were optimized using the CASSCF method with different sizes of the active spaces and mixed by spin−orbit coupling in RASSI. Furthermore, XMS-CASPT2 was extended for each Co site to account for the dynamical electron correlation effects. The central Co1 in **2** lies in a near-octahedral ligand field environment, meaning that the ground state originates from the $^4T_1$ term of the perfect octahedral symmetry. This $^4T_1$ term is subjected to axial and rhombic splitting and on-site spin−orbit coupling effects. These effects are fully considered in the performed *ab initio* calculations. The spin−orbit interaction within the $^4T_1$ term gives rise to 6 (six) Kramers doublets (Table S10), displaying an energy splitting of about 1200−1400 cm^{-1}. As a result of the relatively large orbital contribution—the magnetic anisotropy of the central Co1 site is quite strong. As shown in Table S11, the g tensor of the ground Kramers doublet is strongly axial, defining the orientation of the local magnetic axis as nearly collinear to the Co−Co−Co axis (Figure S19). The Co2 sites lie in an axially distorted tetrahedral ligand field environment. The ground state is an orbitally nondegenerate $^4A_2$ state. To a certain extent, the low-symmetry components of the crystal field and spin−orbit coupling admix excited states, giving rise to a zero-field splitting effect, which splits the ground $^4A_2$ into two Kramers doublets (Table S14). The

https://doi.org/10.1021/acs.cgd.5c00037
Cryst. Growth Des. 2025, 25, 7085−7096

magnetic anisotropy of Co2 sites is weaker than that of the central Co1 site due to a much weaker orbital contribution. The calculated zero-field splitting parameters (D and E) are smaller for Co2 than in central Co1 (cf. Tables S12 and S16). We note the significant effect of the dynamic electron correlation for the zero-field splitting parameters on all of the Co sites. While the CASSCF/RASSI method predicts negative signs of axial anisotropy, the CASPT2/RASSI calculations return positive D values. Despite the change in the sign of parameter D, the orientation of the ground-state magnetic axes remains unchanged, i.e., they are nearly parallel to the Co−Co−Co axis (Figure S19). The origin of their large negative values, e.g., −100 cm^{-1} for Co1 and −29 cm^{-1} for Co2, is also explained (cf. Table S13 and S17). The d-orbital splitting energies for both the central and terminal Co^{II} ions are shown in Figure 3.

The third goal of the theoretical investigation was to establish the strength of the magnetic interaction between the Co sites. For this purpose, broken-symmetry density functional theory (BS-DFT) calculations were performed to estimate exchange coupling parameters (J) and (J') for the exchange Hamiltonian:

$$\hat{H}_{exch} = -J(\hat{S}_{Co1}\hat{S}_{Co2} + \hat{S}_{Co1}\hat{S}_{Co2'}) - J'\hat{S}_{Co2}\hat{S}_{Co2'} \quad (1)$$

Even though the computed values depend on the choice of the DFT functional employed, the values reported in Table S18 show a strong ferromagnetic interaction between Co1 and Co2, ranging between 7 and 12 cm^{-1}. In contrast, the magnetic exchange between the edges (Co2 and Co2′) is predicted by DFT to be significantly weaker (about −0.02 cm^{-1}).

As an alternative to the BS-DFT estimation of the magnetic exchange, POLY-ANISO calculations were carried out. This approach describes the magnetic exchange interaction between metal sites using a single parameter for each metal pair. The Lines exchange Hamiltonian is expanded on the basis of the products of *ab initio* calculated spin−orbit eigenstates of individual Co sites. The magnetic dipole−dipole interaction is added to the exchange coupling by using the *ab initio* computed magnetic dipole moment operators. The diagonalization of the total magnetic Hamiltonian returns the energy exchange states of the entire Co_3 compound; all magnetic properties of the entire Co_3 are computed by using the obtained exchange states. The Lines parameters of magnetic exchange interactions are calibrated solely to minimize the standard deviation between the measured and calculated magnetic susceptibility. The best-fitting parameters reveal FM exchange coupling between the neighboring Co^{II} ions: $J_{Co1-Co2} = J_{Co1-Co2'} = +10.180$ cm^{-1} and $J_{Co2-Co2'} = -0.06$ cm^{-1}, whereas the parameter of intermolecular interaction was found to be $zJ' = -0.0047$ cm^{-1}. It is noteworthy that the semi*ab initio* methodology employed to model magnetic properties, utilizing on-site *ab initio* wave functions, imposes considerable constraints in comparison to the classical ligand field fitting of magnetism, as it limits the on-site contribution to the magnetic moments. The exchange spectrum of **2**, corresponding to the above-fitted exchange parameter, is shown in Figure 4, and the corresponding energy values are listed in Table S19. The ground exchange states have $g_x = 0.246$, $g_y = 0.672$, and $g_z = 21.377$ for Co1 and $g_x = 0.372$, $g_y = 3.635$, and $g_z = 9.165$ for Co2, where all g_z are nearly parallel to the Co−Co−Co axis. The calculated magnetization results using the Lines model are included as the red solid lines in Figures 5 and S20.

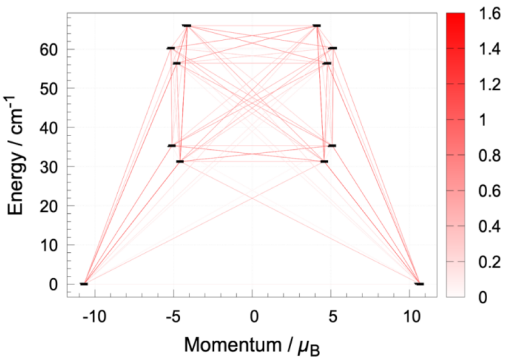

Figure 4. Computed magnetization blocking barrier for **2** using the Lines model of exchange described in the text. The thick black lines represent the low-lying exchange KDs as a function of their magnetic moment along the main anisotropy axis. The intensity of the red lines indicates the relaxation of magnetization.

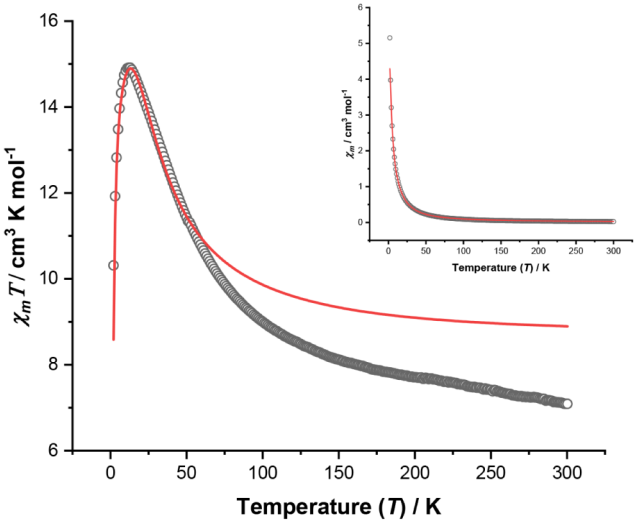

Figure 5. Temperature dependence of $\chi_m T$ vs T plot for complex **2** at 2500 Oe. Inset is χ_m vs T plot. The black circles represent the experimental data, and the red solid lines represent the calculated results using the Lines model, as described in the *Ab Initio* Calculations Section. The possible reasons for the discrepancy are discussed in the main text.

Static Magnetic Properties. All three Co^{II} ions with the electronic configuration [Ar]$3d^7$ are represented by a magnetic center with spin $S = 3/2$. Illustratively, the Co^{II} in tetrahedral coordination (Co2 and Co2′) can be thought to exhibit a high-spin e^4t^3 orbital occupation that is a singlet term with quenched first-order orbital angular momentum, and the Co^{II} in octahedral coordination (Co1) to have a t^5e^2 orbital occupation that is a triplet term with partially unquenched first-order orbital momentum in principle (see the Theoretical Section above for detailed description). All Co ions are in a high-spin state, which is also proven by *ab initio* calculations. The direct-current (dc) magnetic susceptibility product $\chi_m T$ of complex **2** from 2 to 300 K, measured at an applied outer field of 2500 Oe, is shown in Figure 5 (χ_m shown in the inset). A $\chi_m T$ value of 7.088 cm^3 K mol^{-1} at 300 K is significantly higher than the spin-only value ($\chi_m T = 1.875 \times 3 = 5.625$ cm^3 K mol^{-1}) for three isolated and free high-spin Co^{II} metal ions with $g = 2$ and $S = 3/2$, indicating the presence of ferromagnetic (FM) exchange interaction. Due to the FM

https://doi.org/10.1021/acs.cgd.5c00037
Cryst. Growth Des. 2025, 25, 7085−7096

interaction, the $\chi_m T$ value further increases slightly as the temperature is lowered from 300 to 150 K and then reaches the maximum value of 14.913 cm^3 K mol^{-1} at 12 K. Subsequently, the value decreases to 10.311 cm^3 K mol^{-1} at 2 K, likely attributed to the zero-field splitting (ZFS) by single-ion anisotropy effects that reduce the observed net magnetic moment of a polycrystalline sample, especially at low temperature and/or intermolecular antiferromagnetic (AFM) interactions.[19,25] Since the easy magnetic axis is parallel to the Co−Co−Co axis (see *Ab Initio* Calculations) and all these axes are approximately parallel to the crystallographic *c*-axis (Figure S4), a slightly preferred orientation of the needle-like shaped crystals (Figure S2) within the sample container (with the easy-axes perpendicular to the magnetic field direction) might be realized. Due to the strong macroscopic magnetic anisotropy of the crystals, this preferred orientation is supposed to cause a slight reduction of the measured magnetization values in general, which is most pronounced for the low-temperature field scans (Figure S20) but is also present to some extent for the high-temperature susceptibility measurements (Figure 5). The deviation of the fitting curves/parameters with experimental curves, as found in this work, was also reported in the past[29,30] due to the challenges involved in modeling Co^{II}-based molecular magnets, but might additionally be due to the preferred orientation of the small single crystals.

A Curie−Weiss fit according to the law

$$\chi^{-1}(T) = (T - \theta)\cdot C^{-1} \quad (2)$$

with the Curie constant C and the Weiss constant θ has been applied to the inverse susceptibility data of complex **2** to the short temperature range from 275 to 300 K (Figure S16). The fit returns an approximate molar Curie constant of C_{mol} = 5.58(4) cm^3 K mol^{-1} and a Weiss constant θ = +64(2) K. The positive θ value indicates the domination of FM interaction between the adjacent Co1 and Co2 atoms through the $\eta^2{:}\eta^2{:}\mu_3$ siloxane bridges.[26] From the molar Curie constant, an effective magnetic moment of μ_{eff} = 3.86(3) μ_B can be derived as an average value for each of three hypothetically identical magnetic centers (eq S5) that matches with the spin-only value of 3.87 μ_B for a free S = 3/2. Due to contributions from orbital angular momentum to the magnetic moment of Co^{II} ions as indicated from the *ab initio* calculations, actually a somewhat higher experimental value for the effective moment would have been expected. The effect of preferred crystal orientation as outlined above is supposed to be responsible for the fact that only a smaller magnetic moment (corresponding approximately to the spin-only value) has been determined here.

The field (H) dependence of isothermal molar magnetization (M) up to 7 T for various temperatures from 2 to 300 K is shown in Figure S20. At 2 K, the magnetization does not saturate up to 7 T, indicating the presence of single-ion anisotropy that prevents complete alignment of the magnetic moments along the outer field. The magnetization at 7 T (about 4.88 Nμ_B) is significantly lower than the saturation value 9 Nμ_B expected for a system with three free S = 3/2 and g = 2. Still, it is close to the value typically observed for three isolated highly anisotropic Co^{II} ions (3 × 2.21 = 6.63 Nμ_B).[27] Extra isothermal full-loop field scans (measured in sweep mode with 100 Oe s^{-1}) with a maximum field of 20 kOe (2 T) were measured for temperatures ranging from 2 to 5 K (Figure 6). The field scan at 2 K exhibits an open but pinched hysteresis

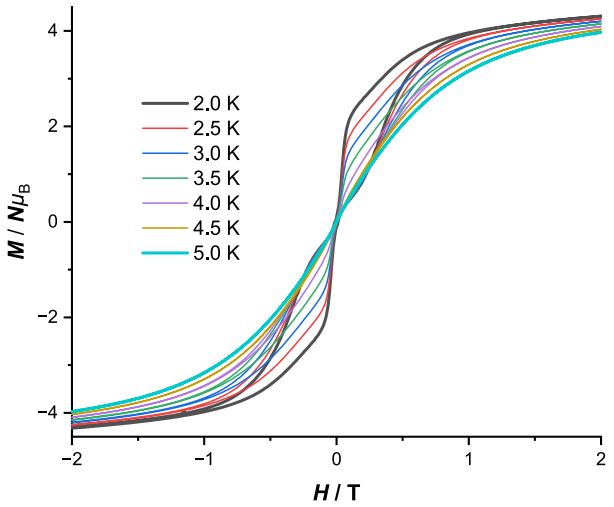

Figure 6. Magnetic hysteresis loop of complex **2** at the indicated temperatures measured in sweep mode at a rate of 100 Oe s^{-1}.

that is narrowed again around the zero field. With increasing temperature, the opening of the hysteresis continuously gets reduced, and at 5 K no clear opening can be observed anymore. Recently, Zabala-Lekuona, Seco, and Colacio et al. have reported a similar Co^{II}_3 complex with a bridging N_3O_3-tripodal Schiff base ligand that exhibits a very similar pinched open hysteresis at 2 K that is however closed again already at 3 K.[19] They reported that the three octahedral Co^{II} ions in their Co^{II}_3 complex exhibit linear antiferromagnetic coupling (S = 3/2, J_{Co-Co} = −6.26(1) cm^{-1}; g_z = 2.826(2), g_{xy} = 2.206(4); D = − 129.6/−116.2 cm^{-1}). Their results about slow magnetic relaxation that has been investigated by ac susceptibility from 3 to 7.6 K will be reconsidered below again when the dynamic magnetic properties are presented and discussed. Another structurally similar ferromagnetically coupled (S = 7/2; J_{Co-Co} = 2.4 cm^{-1}; g_{iso} = 2.48; D_{Co} = − 27.0 cm^{-1}) Co^{II}_3-complex,[25] reported by Zhang and Gao et al., did not show any hysteresis loop for instance.

Dynamic Magnetic Properties. Alternating current (ac) magnetic susceptibility measurements were performed for **2** from 2 to 11 K from 10 Hz to 10 kHz in a zero dc field to gain insight into the dynamics of slow relaxation of magnetization. Most importantly, the out-of-phase χ'' signal exhibits a local maximum that shifts from about 6.5 kHz at 8.5 K to about 100 Hz at 6 K (Figure 7b). The Argand (Cole−Cole) plots in the temperature range of 6−8.5 K are shown in Figure 7c. The ac susceptibility curves were fitted (solid lines) by a generalized Debye model (with the α parameters that describe the distribution of relaxation times ranging from about 0.23 to 0.47), and the relaxation times τ were extracted by using the program CC-Fit2.[28] These relaxation times τ extracted from the ac susceptibility from 6 to 8.5 K are inserted into the ln(τ) vs T^{-1} plot shown in Figure 8. A straight line in the ln(τ) vs T^{-1} plot means that an Arrhenius behavior according to $\tau^{-1} = \tau_0^{-1}\exp(-U_{eff}/k_BT)$ is realized and the corresponding relaxation mechanism is known as the Orbach process (with the slope of the line directly returning U_{eff}). The high-temperature relaxation process (red circles in Figure 8) extracted from the ac susceptibility measurement was linearly fitted with U_{eff} = 94(4) K and τ_0 = 4(2)×10^{-10} s. The value of this Orbach energy barrier is comparable to the absolute height of the *ab initio* computed magnetization blocking barrier for **2**

https://doi.org/10.1021/acs.cgd.5c00037
Cryst. Growth Des. 2025, 25, 7085−7096

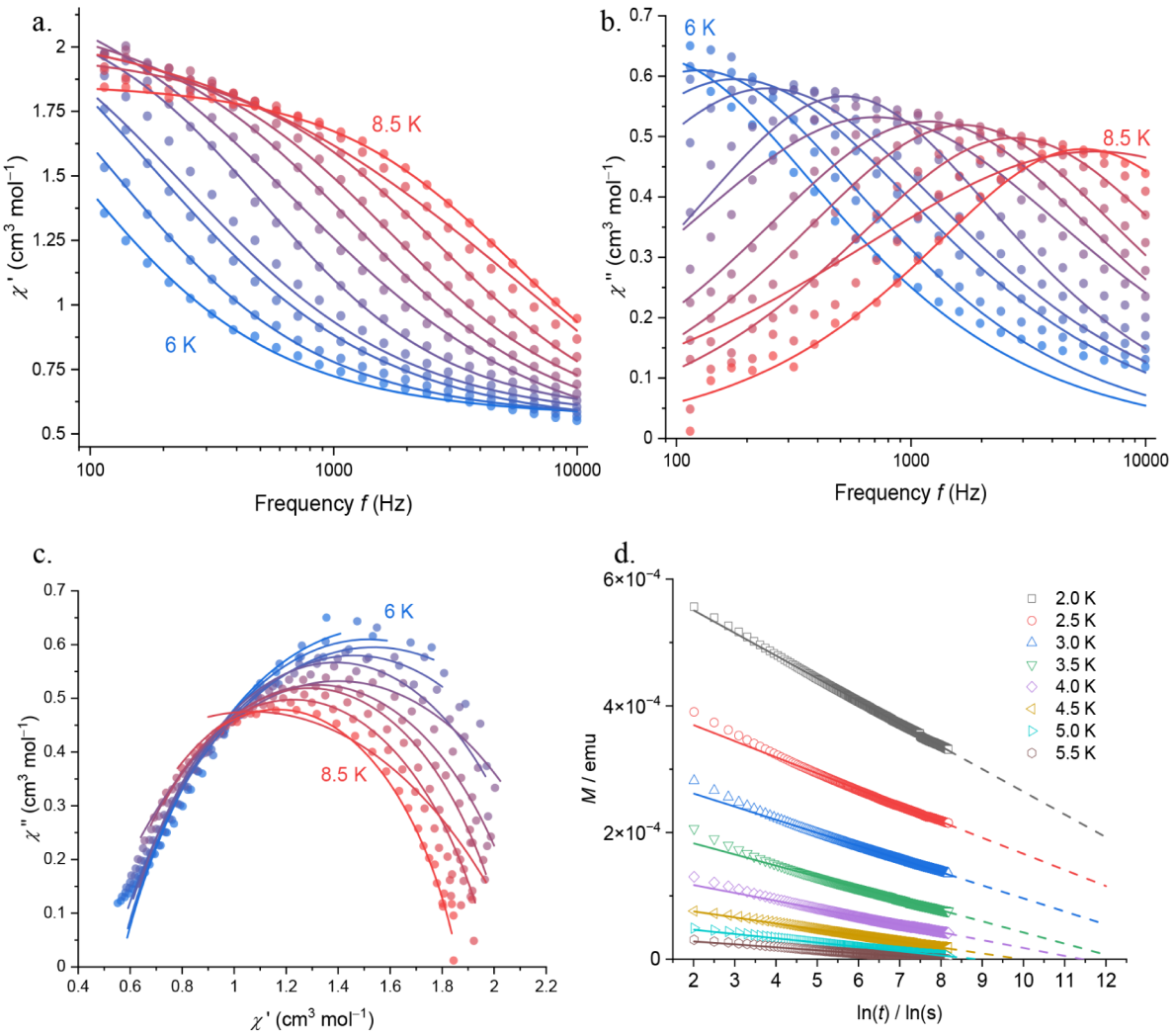

Figure 7. Determination of relaxation times τ from ac susceptibility (a−c) and estimation of relaxation times τ from dc susceptibility (d). In-phase χ' (a) and out-of-phase χ'' (b) components of the ac magnetic susceptibility data for **2**, collected at temperatures of 6−8.5 K with zero-dc applied field and 5 Oe ac excitation field, and Cole−cole plots (χ'' vs χ') (c). The solid lines in (a−c) are generalized Debye functions fitted to the experimental data to extract the relaxation times τ. (d) Logarithmic time evolution of dc magnetization in zero field in the low-temperature region from 2 to 5.5 K. The solid lines represent linear fits that were used to estimate the relaxation times τ from time evolution of dc magnetization.

(see Figure 4) of about 100 K (corresponds to about 70 cm^{-1}). Zabala-Lekuona et al. reported U_{eff} = 43.8(1) K and τ_0 = 6.62(2)×10^{-8} s from the ac susceptibility measurements from 7.6 to 3 K for the similar Co^{II}_3 complex, which possesses three octahedral Co^{II} ions that are connected via phenolate bridges.[19] In principle, the device used for measuring ac susceptibility in the present work with a minimum ac excitation frequency of 10 Hz would allow to follow this Orbach relaxation process down to about 5.7 K (dashed red line in Figure 4) but due to the small available sample amount of only 3.3 mg (single crystals had to be manually collected out of the product for this sample), the ac susceptibility signal below about 100 Hz becomes noisy and for 6 K a reliable determination of the position of the χ'' maximum is not possible anymore (see Figure S22 for a more detailed explanation).

It is a remarkable property of these Co^{II}_3 complexes that the relaxation times are strongly reduced at low temperatures due to the reduction of quantum tunneling (QTM) by FM coupling as also revealed by the low quantum tunneling transition probabilities plotted in Figure 4. The slow magnetic relaxation in this low-temperature region below approximately 5 K, where also a pinched open hysteresis appears, was analyzed by dc magnetometry. Also, the ac susceptibility measurements presented by Zabala-Lekuona et al.[19] were restricted to temperatures above 3 K, i.e., above the temperature where the hysteresis closes. For the dc relaxation experiments applied in this work, the sample was first brought to 2 K before a magnetic field of −1 T (−10 kOe) was set. This field was then set to zero with the highest available rate of 200 Oe s^{-1}. From the time when the magnetic field has reached zero field, the change of the magnetization has been tracked for 1 h. Then, the next higher temperature (0.5 K temperature step size) was set, and the whole procedure was repeated (see the Supporting Information for details). Figure 7d shows the time evolution of the magnetization vs logarithmic time scale from 2 to 5.5 K. The fact that the time evolution can well be approximated by a linear progression in this plot verifies the logarithmic dependence on time. Such a logarithmic time dependence might cover underlying exponential decay with a very broad distribution of relaxation times. From the fitted logarithmic time equations,

https://doi.org/10.1021/acs.cgd.5c00037
Cryst. Growth Des. 2025, 25, 7085−7096

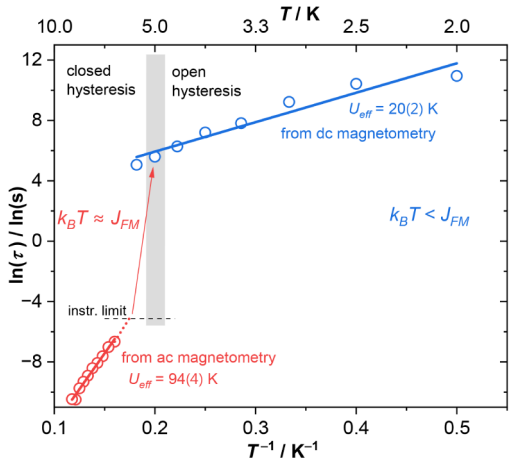

Figure 8. Relaxation times τ determined from ac susceptibility measurements (red circles) and estimated from dc magnetometry (blue circles) in logarithmic ln(τ) vs T^{-1} plot. The solid lines represent fits according to the Arrhenius equation with resulting energy barriers U_{eff}. The dashed black line illustrates the lower frequency limit of the used device to measure ac susceptibility.

the time after which the magnetization has reached 0.37 of its starting value has been used to approximate the relaxation times τ for the low-temperature relaxation process with an overall logarithmic time dependence (for pure exponential decay the relaxation time is defined as the time after which the starting value has decreased to 1/e = 0.37). The obtained approximations for the relaxation times τ for this low-temperature relaxation process are also inserted into the ln(τ) vs T^{-1} plot shown in Figure 8 as blue circles.

Also, these low-temperature relaxation times τ as determined here from the time evolution of the dc magnetization signal (below about 5 K), follow an Arrhenius behavior, and a linear fit returns U_{eff} = 20(2) K and τ_0 = 9(5) s. The relaxation times of that low-temperature process range from about 3 min (exp[5.1] s) at 5.5 K to about 16 h (exp[10.95] s) at 2 K. It should be mentioned that even though these low-temperature relaxation rates follow this Arrhenius behavior, the corresponding relaxation process is not related to what is known as the Orbach relaxation process but simply exhibits a temperature behavior that can be a good approximation described by the same Arrhenius behavior. Since an energy barrier of only U_{eff} = 20(2) K has been determined for this low-temperature relaxation process (below about 5 K), it can be speculated that this relaxation process is present at temperatures where the ferromagnetic coupling between the Co^{II} ions is still dominating. In the theoretical section above, the FM exchange coupling between neighboring Co^{II} ions has been determined to $J_{Co1-Co2} = J_{Co1-Co2'}$ = +10.180 cm^{-1}, which corresponds to an equivalent temperature of J = 14.6 K and is therefore in a similar range as the energy barrier U_{eff} = 20(2) K. As long as this ferromagnetic coupling is dominating at a very low temperature (2−5 K), the open (pinched) hysteresis can be observed, and a very slow magnetic relaxation process is indicated from the results of time-dependent dc magnetometry. Once the ferromagnetic coupling loses its capability to align the neighboring Co ions at a higher temperature (approaching 5 K), the hysteresis is no longer opened, and at a slightly higher temperature (above 6 K) an Orbach relaxation process can be observed. The low-temperature relaxation (blue points) is much slower because it involves coupled spin states of all three Co sites (exchange eigenstates), while the high-temperature relaxation takes place on individual Co sites (uncoupled), where the presence of the neighboring Co sites plays a destructive role, being a source of fluctuating magnetic field in the proximity.

It is worth mentioning that an Orbach relaxation time of about 1 ms has clearly been observed by ac susceptibility at 6.25 K, but that at about 5 K the appearance of the open hysteresis goes together with relaxation times of about 3 min (dc relaxation time at 5.5 K). That means that the relaxation times change over more than 4 orders of magnitude, going from 6.25 to 5.5 K. Unfortunately, the transition from the low-temperature relaxation process (blue circles) to the high-temperature relaxation process (red circles) cannot be tracked here in complete detail. This is because the relaxation times in this transition region are becoming too large to be analyzed by ac susceptibility but they are already too small to be adequately tracked by dc magnetometry (at least with the used PPMS option in this work).

CONCLUSION

We have synthesized and structurally characterized the dianionic linear trinuclear Co^{II}_3 complex **2**, which contains two types of Co^{II} ions with favorable local easy-axis anisotropy of tetrahedral and octahedral Co^{II} ions. The butterfly-like Co^{II}_3-complex **2** has Co−O−Co bridging angles of 97.7(2)° and an intramolecular Co−Co distance of 3.029(2) Å. The adjacent Co^{II} ions are strongly ferromagnetically coupled (J_{Co-Co} = +10.180 cm^{-1}) via four μ-O atoms of two dianionic siloxanes $(Me_4Si_2O_3)^{2-}$ bridges. Stronger charge separation between the O and Si atoms of $Me_4Si_2O_3^{2-}$ provides favorable D of each Co^{II} ion. *Ab initio* calculations showed that the Co^{II} ions possess rhombic anisotropy with near collinearly arrangements of local anisotropy (D_z) along the line connected to all three Co^{II} ions. The QTM is also expected based on the computed values of g [g_x, $g_y \neq 0$] and D tensors.

From ac susceptibility the realization of an Orbach relaxation process with U_{eff} = 94(4) K and $\tau_0 = 4(2)\times10^{-10}$ s could be found for the temperature range from 8.5 to 6.25 K. The value of this Orbach energy barrier is comparable to the absolute height of the *ab initio* computed magnetization blocking barrier for **2** of about 100 K (corresponds to about 70 cm^{-1}). Below about 5 K where also a pinched open hysteresis can clearly be observed, the slow magnetic relaxation has been investigated by time-dependent evolution of the dc magnetization signal after the dc field has been set to zero. A logarithmic time dependence of magnetization has been found with quite large estimated relaxation times ranging from about 3 min at 5.5 K to about 16 h at 2 K which is remarkable. This linear Co^{II}_3-complex (**2**), with Co^{II} ions in two different coordination geometries, possesses very high relaxation times at low temperature compared to other previously reported Co^{II}_3 based[19,25] single-molecule magnets. In the temperature range (below about 5.5 K), where the FM coupling is dominating, the magnetic relaxation is strongly suppressed (low quantum tunneling probability), leading even to the pinched open hysteresis. At higher temperatures (slightly above 6 K), the FM coupling is not dominating anymore, and the relaxation process again has more individual ion character and occurs via an Orbach relaxation process with much smaller relaxation times.

https://doi.org/10.1021/acs.cgd.5c00037
Cryst. Growth Des. 2025, 25, 7085−7096

EXPERIMENTAL SECTION

General Remarks. All manipulations were carried out under an atmosphere of dry, O_2-free vacuum employing inert argon (Ar) gas-filled MBraun Eco Plus glove box. All glassware was oven-dried (150 °C) before use. Reactions and further work up are carried out under a dry argon atmosphere using standard Schlenk line vacuum techniques. Prior to use, solvents were distilled under an Ar atmosphere according to the literature procedure and kept under an Ar-filled atmosphere into thick-walled Schlenk storage flasks equipped with Teflon-valve stopcocks. All of the chemicals and other solvents were purchased from local companies. The chemicals were treated with vacuum and argon flow cycles and stored inside an Ar-filled glove box. Benzene, THF, and toluene were distilled successively from purple sodium benzophenone ketyl and Na/K alloy. Ethyl acetate was distilled with dry CaH_2 and stored with activated 4 Å zeolite molecular sieves. Methanol was distilled with Mg turnings and I_2, and the distilled solvent was stored with activated 3 Å zeolite molecular sieves. All the zeolite molecular sieves were precalcined at 300 °C for at least 12 h and then under flowing argon at 150 °C for 4 h.

Synthesis Procedure. Methylene diphosphonium bromide salt, as the starting material for of CDP, was prepared following the reported methodology of Matthews et al.[29]

Synthesis of Hexaphenylcarbodiphosphorane (CDP) (1). Methylenebis(triphenylphosphonium) dibromide (1.43 mmol, 1 g) and lithium diisopropylamide (Li[N(^{i}Pr)$_2$], LDA) (2.86 mmol, 307 mg) were combined in tetrahydrofuran (THF, 20 mL) in a 250 mL Schlenk flask. The reaction mixture immediately became yellow in color and was stirred for 30 min at room temperature. Subsequently, the volatile components like diisopropylamine (HN(^{i}Pr)$_2$) were removed under high vacuum. Toluene (80 mL) was added to the resultant yellow solid, and the mixture was filtered using a G-4 frit to remove LiBr. The yellow CDP filtrate obtained was dried under a high vacuum (690 mg, 90%). Spectroscopic data of the product are identical to those previously reported.[29]

Synthesis of Complex [(HCDP)$_2$Co$^{II}_3$(sil)$_2$Cl$_4$(THF)$_2$]·4THF (2). Carbodiphosphorane (CDP) (**1**) (0.5 mmol, 268 mg) was placed in a 100 mL Schlenk flask, and toluene (15 mL) was added via a cannula at room temperature (rt) to obtain a transparent yellow solution. The resultant solution was passed to a 100 mL Schlenk flask containing microcrystalline blue powders of $CoCl_2(PPh_3)_2$ (0.5 mmol, 327 mg) at rt. A clear dark green solution was obtained on stirring for a couple of minutes, and then the color was changed to purple due to the formation of a small amount of faded blue precipitate (Scheme 1), which was further precipitated out in larger quantity on stirring for additional 4 h resulting decrease in the intensity of the purple color solution. The faded blue-colored precipitate was filtered using a frit. The resultant precipitate was reacted in THF with another 2 equiv of CDP in THF, forming greenish-blue needles of complex **2** in 20% yield. Elemental analysis found (calculated) [%]: C 60.11 (60.02), H 6.72 (6.77) matching with $C_{122}H_{164}Cl_4Co_3O_{16}P_4Si_4$ (**2** with an additional 4 THF molecules).

Analytical Techniques. *Single-Crystal X-ray Diffraction (SC-XRD) Analysis.* The crystals were picked up with a spatula, placed into frozen paratone oil on a glass slide, and mounted under an argon flow. The average data collection time was 8−12 h for a single crystal under the flow of liquid nitrogen at 150 K. Single crystal X-ray diffraction data were collected on a Bruker D8 Venture APEX4 HEED diffractometer, equipped with a PHOTON III C28 detector using an IμS 3.0 microfocus sealed X-ray source with Helios optics monochromatic Mo−Kα (λ = 0.71073 Å) radiation at 150 K. Complete data set was collected following the strategies generated using the APEX4[30] module of the Bruker software suite. The data reduction and integration were carried out using SAINTPLUS.[31] Multiscan absorption correction was performed using the program SADABS.[32] The crystal structures were solved by the intrinsic phasing method SHELXT[33] and were refined with full-matrix least-squares on F2 using ShelXle[34] plug-in included in APEX4. All of the hydrogen atoms were added at calculated positions and refined using a riding model. Their isotropic temperature factors were fixed to 1.2 times (1.5 times for methyl groups) the equivalent isotropic displacement parameters of the parent carbon atom. Anisotropic thermal displacement parameters were used for all the nonhydrogen atoms.

UV−Visible Spectroscopy. UV−visible spectra were recorded in a Jasco V-650 spectrophotometer using standard quartz cuvettes (1 cm × 1 cm cross-section) in the 350−900 nm range at room temperature in THF solvent.

Fourier-Transform Infrared (FT-IR) Spectroscopy. FT-IR spectra were recorded for the solid samples using KBr pellets on a Jasco FT/IR-4100 spectrometer in the 400−4000 cm^{-1} range. A small quantity of infrared-grade potassium bromide (KBr), sufficient to cover an area of approximately 20 mm^2 to a depth of 1 mm, was placed in mortars. A small aliquot of the powdered sample was then combined with KBr and subjected to grinding to ensure homogeneous distribution throughout the mixture. Subsequently, a pellet was formed, and FT-IR spectra were obtained.

Nuclear Magnetic Resonance (NMR) Spectroscopy. ^{1}H, ^{13}C, ^{31}P, and ^{29}Si NMR spectra were recorded on a Bruker Avance III 500 MHz NMR spectrometer. Chemical shifts (δ) are reported in parts per million (ppm), are given relative to $SiMe_4$, and are referenced to the residual solvent signal to $CDCl_3$ at 7.19 ppm (^{1}H NMR) and 76.88 ppm (^{13}C NMR).

Electron Paramagnetic Resonance (EPR) Spectroscopy. EPR spectra were obtained using an X-band (8.75−9.65 GHz) JEOL Model JES FA200 EPR spectrometer at 298 and 77 K in DMSO medium.

Powder X-ray Diffraction (PXRD). The PXRD pattern was examined using Cu Kα (0.154 nm) radiation on a Rigaku Miniflex 600C diffractometer, spanning a range of 2θ values from 5° to 80°.

Thermogravimetric Analysis (TGA). TGA was performed in the temperature range of 30 to 1100 °C on STARe Default DB V18.00: Mettler-Toledo instrument with 12.94 mg of crystalline sample loaded on an Al crucible.

Magnetic Measurements. Direct current (dc) magnetization was measured with a physical property measurement system (PPMS) DynaCool from Quantum Design equipped with a vibrating sample magnetometry (VSM) option. 3.3 mg of the crystalline sample **2** was pressed into a polypropylene capsule (P125E from Quantum Design) and attached to the brass half-tube sample holder (C130B from Quantum Design). The single crystals of **2** (Figure S2) used for magnetic measurements were manually picked inside the glove box. The dc magnetization vs temperature was measured at a magnetic field of 2500 Oe from 2 to 50 K in settle mode and from 51 to 300 K in sweep mode with a 1 K/min heating rate. The temperature step size for signal acquisition was 1 K with a signal averaging time of 10 s. Magnetization vs field was measured at 2, 3, 4, 6, 10, 15, 25, 50, and 300 K up to 7 T with a field step size of 2500 Oe (0.25 T), a signal averaging time of 10 s, and a 2-fold redundancy per measuring point. At each temperature, the magnetic field was first increased to 7 T and then the field was decreased to zero field again. The superimposed curves for all field scans verified that no reorientation of the sample's powder particles had been induced by the magnetic field. The magnetic dc raw data of the so far described measurements have been corrected for diamagnetic contributions (except for the full loop sweep scans) from the atomic closed shells and from the bonding electrons (as listed in Table S5) according to the incremental method.[35]

Furthermore, full hysteresis loops with a maximum field of 20 kOe (2 T) have been measured from 2 to 5 K with an incremental temperature step size of 0.5 K in sweep mode with a rate of 100 Oe s^{-1}. The sample was cooled down in field-cool mode at −2 T to 2 K. Then the full loop hysteresis was measured and the next temperature was then set while the field of −2 T was held. To estimate the comparably large relaxation times at low temperatures (below about 5 K), the evolution of the magnetization has been tracked over time after the magnetic field has been set from −1 T to zero magnetic field with the highest available rate of 200 Oe s^{-1}. The details of these time-dependent dc magnetization measurements are outlined in Figures S17 and S18.

https://doi.org/10.1021/acs.cgd.5c00037
Cryst. Growth Des. 2025, 25, 7085−7096

The ac susceptibility was measured first with an ACMS-II option from 10 Hz to 10 kHz at 35 frequencies with log-distribution at 0, 500, 1000, and 1500 Oe dc field at 2 K (Figure S21). Only the ac measurement at zero dc field exhibits a significant χ'' signal strength that points to the realization of slow magnetic relaxation. Already at 500 Oe, the total ac signal has reduced so strongly that ac measurements at higher fields could not be performed here (a reason for the weak signal is also the small available sample mass of only 3.3 mg). Therefore, ac susceptibility was measured from 10 Hz to 10 kHz at 35 frequencies with log-distribution from 2 to 11 K at zero dc field. For temperatures above about 6 K (Figure S22), a clear maximum of the imaginary χ'' can be observed for frequencies above 100 Hz and the corresponding relaxation times could be determined (by using the program CC-Fit2) for the temperature range from 6.25 to 8.5 K. For the ac measurements, the polypropylene sample capsule was attached to the polymer straw sample holder (AGC2 from Quantum Design) with the help of some polyimid tape. The ac excitation field was 5 Oe with an average time per measuring point of 10 s. The ac raw data sets have not been corrected for diamagnetic contributions.

Theoretical Calculations. Density functional theory calculations were done for several purposes: to establish the ground state total spin of the entire Co_3 unit, to establish the ground state of individual Co ions in the Co_3 unit, and to estimate the magnetic interaction between Co sites. All density functional theory (DFT) calculations were done using the ORCA 5.0.4 software package.[24] The computed molecular structures were based on the crystal structure derived from X-ray diffraction analysis. All atoms were described using def2-SVP basis sets. All DFT calculations employed the spin-unrestricted formalism (UKS). The convergence thresholds for the DFT calculations were set by the "VeryTightSCF" keyword, supplemented by the DEFGRID3 option, which enables a dense density integration grid. Resolution of identity was used for all DFT calculations with generation on the fly of the auxiliary basis sets enabled by the "autoaux" option. To calculate the magnetic coupling between the neighboring Co^{II} centers by substituting the other Co^{II} ion with a diamagnetic Zn^{II} ion (Co−Co−Zn complex), broken-symmetry (BS) DFT was performed (Table S18). All DFT calculations used four DFT functionals: B3LYP, PBE, TPSS0, and wB97.

The electronic structure and magnetic properties have been computed by *ab initio* multiconfigurational CASSCF/CASPT2 calculations with the OpenMOLCAS package.[23] All atoms were described by ANO-RCC basis sets.[36] Scalar relativistic corrections were accounted for using the Douglas−Kroll−Hess procedure.[37] The active space chosen for the CASSCF calculation was CAS(7,10), where $3d^7$ electrons were considered in 10 orbitals (five 3d + five 4d) orbitals. All the roots arising from quartet ($S = 3/2$) and doublet ($S = 1/2$) multiplicities for $3d^7$ configuration were considered, i.e., 10 quartet roots from (^4F, ^4P) and 40 doublet roots (^2G, ^2P, ^2H, ^2D, ^2D, ^2F) (Tables S10−S17). Extended multistate XMS-CASPT2 calculations were done to account for the missing dynamic electron correlation and improve the overall results.[38] The atomic mean-field approximation (AMFI) was used in RASSI to approximate the spin−orbit interaction.[39] The SINGLE_ANISO program calculated the spin-Hamiltonian parameters (*g*-tensor, *D*-tensor, *D*, and *E* parameters). The POLY_ANISO program used the *ab initio* results of the CASPT2-VTZP to calculate the overall magnetic susceptibility at 2500 Oe (Figure 5), magnetization (Figure S20), and *ab initio* blocking barrier (Figure 4) using the Lines exchange model to describe magnetic coupling between Co sites.[40]

■ ASSOCIATED CONTENT

Supporting Information

The Supporting Information is available free of charge at https://pubs.acs.org/doi/10.1021/acs.cgd.5c00037.

Supporting Information (summarized in a pdf) provides complete information on the full molecular structure and crystal packing of complex **2**, crystallographic details, UV−visible, IR, ESI-HRMS, EPR, PXRD, TGA, NMR and further computational data. It contains *ab initio* theoretical calculations result on ground state optimization for the Co_3 dianion, Loewdin charge and spin population analysis, multireference calculations for individual Co sites in Co_3 dianion, ZFS parameters and *g* tensors, broken-symmetry evaluation of the magnetic exchange interactions in Co_3, POLY-ANISO results, ac susceptibility data, etc. In addition, cif file of the crystal structure is also available (PDF)

Accession Codes

Deposition Number 2415240 contains the supplementary crystallographic data for this paper. These data can be obtained free of charge via the joint Cambridge Crystallographic Data Centre (CCDC) and Fachinformationszentrum Karlsruhe Access Structures service.

■ AUTHOR INFORMATION

Corresponding Authors

Kartik Chandra Mondal − *Department of Chemistry, Indian Institute of Technology Madras, Chennai 600036, India;* orcid.org/0000-0002-5830-3608; Email: csdkartik@iitm.ac.in

Björn Schwarz − *Institute for Applied Materials (IAM), Karlsruhe Institute of Technology (KIT), Eggenstein-Leopoldshafen 76344, Germany;* orcid.org/0000-0002-9461-1448; Email: bjoern.schwarz@kit.edu

Liviu Ungur − *Department of Chemistry, National University of Singapore, Singapore 119077, Singapore;* orcid.org/0000-0001-5015-4225; Email: chmlu@nus.edu.sg

Authors

Madhuri Bhattacharya − *Department of Chemistry, Indian Institute of Technology Madras, Chennai 600036, India;* orcid.org/0000-0003-4203-3735

Sunil Kumar − *Department of Chemistry, Indian Institute of Technology Madras, Chennai 600036, India;* orcid.org/0000-0003-3418-4314

Complete contact information is available at: https://pubs.acs.org/10.1021/acs.cgd.5c00037

Author Contributions

M.B. performed synthesis, crystallization, and other experimental studies. L.U. did the magnetic simulations and B.S. performed the corresponding experimental studies. S.K. helped in interpreting computational results. M.B. wrote the first draft of the manuscript, and all the coauthors contributed to finalizing it. K.C.M. conceptualized the work and supervised and finalized the manuscript.

Notes

The authors declare no competing financial interest.

■ ACKNOWLEDGMENTS

The authors thank IIT Madras for the laboratory and SAIF-IIT Madras for the advanced equipment. We thank IISER Tirupati for their low-temperature SC-XRD machine facility. M.B. thanks the Ministry of Education, Govt. of India, for the Prime Minister's Research Fellows (PMRF) research grant #SB22230907CYPMRF008694, which supported her fellowship. L.U. acknowledges the financial support of the research projects A-800079-00-00, A-8000017-00-00, and A-8001894-00-00 of the National University of Singapore. *Ab initio* calculations were done on the ASPIRE-2A cluster (www.nscc.

sg) under project 11004127. This work used computational resources of the supercomputer Fugaku provided by RIKEN/NSCC through the HPCI System Research Project (Project ID: hp240202). The computational resources of the HPC-NUS are gratefully acknowledged. K.C.M. gratefully acknowledges the funding by SERB, New Delhi for ECR grants (ECR/2016/000890) and IIT Madras for the seed grant. This work is dedicated to Prof. Sanjay Kumar, IIT Madras.

REFERENCES

(1) Frost, J. M.; Harriman, K. L. M.; Murugesu, M. The Rise of 3-d Single-Ion Magnets in Molecular Magnetism: Towards Materials from Molecules? *Chem. Sci.* **2016**, *7*, 2470−2491.
(2) Rechkemmer, Y.; Breitgoff, F. D.; Van Der Meer, M.; Atanasov, M.; Hakl, M.; Orlita, M.; Neugebauer, P.; Neese, F.; Sarkar, B.; Van Slageren, J. A Four-Coordinate Cobalt(II) Single-Ion Magnet with Coercivity and a Very High Energy Barrier. *Nat. Commun.* **2016**, *7* (1), 10467.
(3) Mannini, M.; Pineider, F.; Danieli, C.; Totti, F.; Sorace, L.; Sainctavit, P.; Arrio, M.-A.; Otero, E.; Joly, L.; Cezar, J. C.; Cornia, A.; Sessoli, R. Quantum Tunnelling of the Magnetization in a Monolayer of Oriented Single-Molecule Magnets. *Nature* **2010**, *468*, 417−421.
(4) Leuenberger, M. N.; Loss, D. Quantum Computing in Molecular Magnets. *Nature* **2001**, *410*, 789−793.
(5) Bogani, L.; Wernsdorfer, W. Molecular Spintronics Using Single-Molecule Magnets. *Nat. Mater.* **2008**, *7*, 179−186.
(6) Milios, C. J.; Vinslava, A.; Wernsdorfer, W.; Moggach, S.; Parsons, S.; Perlepes, S. P.; Christou, G.; Brechin, E. K. A Record Anisotropy Barrier for a Single-Molecule Magnet. *J. Am. Chem. Soc.* **2007**, *129*, 2754−2755.
(7) Boyd, P. D. W.; Li, Q.; Vincent, J. B.; Folting, K.; Chang, H. R.; Streib, W. E.; Huffman, J. C.; Christou, G.; Hendrickson, D. N. Potential Building Blocks for Molecular Ferromagnets: $[Mn_{12}O_{12}(O_2CPh)_{16}(H_2O)_4]$ with a S = 14 Ground State. *J. Am. Chem. Soc.* **1988**, *110* (25), 8537−8539.
(8) Chiesa, A.; Cugini, F.; Hussain, R.; Macaluso, E.; Allodi, G.; Garlatti, E.; Giansiracusa, M.; Goodwin, C. A. P.; Ortu, F.; Reta, D.; et al. Understanding Magnetic Relaxation in Single-Ion Magnets with High Blocking Temperature. *Phys. Rev. B* **2020**, *101* (17), 174402.
(9) Waldmann, O. A Criterion for the Anisotropy Barrier in Single-Molecule Magnets. *Inorg. Chem.* **2007**, *46*, 10035−10037.
(10) Woodruff, D. N.; Winpenny, R. E. P.; Layfield, R. A. Lanthanide Single-Molecule Magnets. *Chem. Rev.* **2013**, *113*, 5110−5148.
(11) Blagg, R. J.; Ungur, L.; Tuna, F.; Speak, J.; Comar, P.; Collison, D.; Wernsdorfer, W.; McInnes, E. J. L.; Chibotaru, L. F.; Winpenny, R. E. P. Magnetic Relaxation Pathways in Lanthanide Single-Molecule Magnets. *Nat. Chem.* **2013**, *5*, 673−678.
(12) Le Roy, J. J.; Jeletic, M.; Gorelsky, S. I.; Korobkov, I.; Ungur, L.; Chibotaru, L. F.; Murugesu, M. An Organometallic Building Block Approach To Produce a Multidecker 4 *f* Single-Molecule Magnet. *J. Am. Chem. Soc.* **2013**, *135*, 3502−3510.
(13) Guo, F.-S.; Day, B. M.; Chen, Y.-C.; Tong, M.-L.; Mansikkamäki, A.; Layfield, R. A. Magnetic Hysteresis up to 80 K in a Dysprosium Metallocene Single-Molecule Magnet. *Science* **2018**, *362*, 1400−1403.
(14) Liu, F.; Velkos, G.; Krylov, D. S.; Spree, L.; Zalibera, M.; Ray, R.; Samoylova, N. A.; Chen, C.-H.; Rosenkranz, M.; Schiemenz, S.; et al. Air-stable redox-active nanomagnets with lanthanide spins radical-bridged by a metal−metal bond. *Nat. Commun.* **2019**, *10* (1), 571.
(15) Gould, C. A.; McClain, K. R.; Reta, D.; Kragskow, J. G. C.; Marchiori, D. A.; Lachman, E.; Choi, E.-S.; Analytis, J. G.; Britt, R. D.; Chilton, N. F.; Harvey, B. G.; Long, J. R. Ultrahard Magnetism from Mixed-Valence Dilanthanide Complexes with Metal-Metal Bonding. *Science* **2022**, *375*, 198−202.
(16) Barra, A. L.; Caneschi, A.; Cornia, A.; Fabrizi De Biani, F.; Gatteschi, D.; Sangregorio, C.; Sessoli, R.; Sorace, L. Single-Molecule Magnet Behavior of a Tetranuclear Iron(III) Complex. The Origin of Slow Magnetic Relaxation in Iron(III) Clusters. *J. Am. Chem. Soc.* **1999**, *121*, 5302−5310.
(17) Boča, R.; Rajnák, C.; Titiš, J.; Valigura, D. Field Supported Slow Magnetic Relaxation in a Mononuclear Cu(II) Complex. *Inorg. Chem.* **2017**, *56*, 1478−1482.
(18) Miklovič, J.; Valigura, D.; Boča, R.; Titiš, J. A Mononuclear Ni(II) Complex: A Field Induced Single-Molecule Magnet Showing Two Slow Relaxation Processes. *Dalton Trans.* **2015**, *44*, 12484−12487.
(19) Zabala-Lekuona, A.; Landart-Gereka, A.; Quesada-Moreno, M. M.; Mota, A. J.; Díaz-Ortega, I. F.; Nojiri, H.; Krzystek, J.; Seco, J. M.; Colacio, E. Zero-Field SMM Behavior Triggered by Magnetic Exchange Interactions and a Collinear Arrangement of Local Anisotropy Axes in a Linear Co_3^{II} Complex. *Inorg. Chem.* **2023**, *62*, 20030−20041.
(20) Oldengott, J.; Stammler, A.; Bögge, H.; Glaser, T. Enhancing the Ferromagnetic Coupling in Extended Phloroglucinol Complexes by Increasing the Metal SOMO−Ligand Overlap: Synthesis and Characterization of a Trinuclear Co^{II}_3 Triplesalophen Complex. *Dalton Trans.* **2015**, *44*, 9732−9735.
(21) Mocanu, M. I.; Patrascu, A. A.; Hillebrand, M.; Shova, S.; Lloret, F.; Julve, M.; Andruh, M. Trinuclear Nickel(II) and Cobalt(II) Complexes Constructed from Mannich−Schiff-Base Ligands: Synthesis, Crystal Structures, and Magnetic Properties. *Eur. J. Inorg. Chem.* **2019**, *2019*, 4773−4783.
(22) Monakhov, K. Y.; van Leusen, J.; Kögerler, P.; Zins, E.; Alikhani, M. E.; Tromp, M.; Danopoulos, A. A.; Braunstein, P. L. Linear, Trinuclear Cobalt Complexes with *o* -Phenylene-bis-Silylamido Ligands. *Chem.−Eur. J.* **2017**, *23* (27), 6504−6508.
(23) Li Manni, G.; Fdez. Galván, I.; Alavi, A.; Aleotti, F.; Aquilante, F.; Autschbach, J.; Avagliano, D.; Baiardi, A.; Bao, J. J.; Battaglia, S.; et al. The OpenMolcas Web: A Community-Driven Approach to Advancing Computational Chemistry. *J. Chem. Theory Comput.* **2023**, *19* (20), 6933−6991.
(24) Neese, F. Software update: The ORCA program system—Version 5.0. *Wiley Interdiscip. Rev.: Comput. Mol. Sci.* **2022**, *12* (5), No. e1606.
(25) Zhang, Y.-Z.; Brown, A. J.; Meng, Y.-S.; Sun, H.-L.; Gao, S. Linear Trinuclear Cobalt(II) Single Molecule Magnet. *Dalton Trans.* **2015**, *44*, 2865−2870.
(26) Yang, Y.-T.; Zhao, F.-H.; Che, Y.-X.; Zheng, J.-M. A Unique Mixed-Bridged Trinuclear Co (II) Complex and Its Extended System: Structural and Magnetic Studies. *Inorg. Chem. Commun.* **2011**, *14*, 1802−1806.
(27) Kumar, S.; Arumugam, S.; Schwarz, B.; Ehrenberg, H.; Mondal, K. C. Static and Dynamic Magnetic Properties of a Co(II)-Complex with N 2 O 2 Donor Set − A Theoretical and Experimental Study. *Eur. J. Inorg. Chem.* **2023**, *26* (10), No. e202200774.
(28) Reta, D.; Chilton, N. F. Uncertainty Estimates for Magnetic Relaxation Times and Magnetic Relaxation Parameters. *Phys. Chem. Chem. Phys.* **2019**, *21*, 23567−23575.
(29) Driscoll, J. S.; Grisley Jr, D. W.; Pustinger, J. V.; Harris, J. E.; Matthews, C. N. Properties and Reactions of Mesomeric Phosphonium Salts1. *J. Org. Chem.* **1964**, *29*, 2427−2431.
(30) Bruker *APEX4. Bruker Nano, Inc.*, Madison, WI, USA: Bruker Nano, Inc., 2021.
(31) Bruker *SAINT V8.40B*: Bruker AXS LLC. 2019.
(32) Krause, L.; Herbst-Irmer, R.; Sheldrick, G. M.; Stalke, D. Comparison of Silver and Molybdenum Microfocus X-Ray Sources for Single-Crystal Structure Determination. *J. Appl. Crystallogr.* **2015**, *48*, 3−10.
(33) Sheldrick, G. M. *SHELXT* − Integrated Space-Group and Crystal-Structure Determination. *Acta Crystallogr. Sect. Found. Adv.* **2015**, *71*, 3−8.
(34) Hübschle, C. B.; Sheldrick, G. M.; Dittrich, B. ShelXle: A Qt Graphical User Interface for *SHELXL*. *J. Appl. Crystallogr.* **2011**, *44*, 1281−1284.

https://doi.org/10.1021/acs.cgd.5c00037
Cryst. Growth Des. 2025, 25, 7085−7096

(35) Bain, G. A.; Berry, J. F. Diamagnetic Corrections and Pascal's Constants. *J. Chem. Educ.* **2008**, *85*, 532.
(36) Roos, B. O.; Lindh, R.; Malmqvist, P.-Å.; Veryazov, V.; Widmark, P.-O. New Relativistic ANO Basis Sets for Transition Metal Atoms. *J. Phys. Chem. A* **2005**, *109*, 6575−6579.
(37) Reiher, M. Douglas−Kroll−Hess Theory: A Relativistic Electrons-Only Theory for Chemistry. *Theor. Chem. Acc.* **2006**, *116*, 241−252.
(38) Granovsky, A. A. Extended Multi-Configuration Quasi-Degenerate Perturbation Theory: The New Approach to Multi-State Multi-Reference Perturbation Theory. *J. Chem. Phys.* **2011**, *134* (21), 214113.
(39) Malmqvist, P. Å.; Roos, B. O.; Schimmelpfennig, B. The Restricted Active Space (RAS) State Interaction Approach with Spin−Orbit Coupling. *Chem. Phys. Lett.* **2002**, *357*, 230−240.
(40) Chibotaru, L. F.; Ungur, L. *Program POLY_ANISO*; KU Leuven: Leuven, Belgium, 2007.

https://doi.org/10.1021/acs.cgd.5c00037
Cryst. Growth Des. 2025, 25, 7085−7096